Supplementary information for "Singlet-doublet transitions of a quantum dot Josephson junction revealed in a transmon circuit"

Arno Bargerbos,[1,*] Marta Pita-Vidal,[1,*] Rok Žitko,[2,3] Jesús Ávila,[4] Lukas J. Splitthoff,[1] Lukas Grünhaupt,[1] Jaap J. Wesdorp,[1] Christian K. Andersen,[1] Yu Liu,[5] Leo P. Kouwenhoven,[1] Ramón Aguado,[4] Angela Kou,[6] and Bernard van Heck[7]

[1] *QuTech and Kavli Institute of Nanoscience, Delft University of Technology, 2600 GA Delft, The Netherlands*
[2] *Jožef Stefan Institute, Jamova 39, SI-1000 Ljubljana, Slovenia*
[3] *Faculty of Mathematics and Physics, University of Ljubljana, Jadranska 19, SI-1000 Ljubljana, Slovenia*
[4] *Instituto de Ciencia de Materiales de Madrid (ICMM), Consejo Superior de Investigaciones Cientificas (CSIC), Sor Juana Ines de la Cruz 3, 28049 Madrid, Spain*
[5] *Center for Quantum Devices, Niels Bohr Institute, University of Copenhagen, 2100 Copenhagen, Denmark*
[6] *Department of Physics and Frederick Seitz Materials Research Laboratory, University of Illinois Urbana-Champaign, Urbana, IL 61801, USA*
[7] *Leiden Institute of Physics, Leiden University, Niels Bohrweg 2, 2333 CA Leiden, The Netherlands*

(Dated: May 23, 2022)

CONTENTS

---

* These two authors contributed equally.

I. NUMERICAL MODELING

A. Anderson model with superconducting leads

As discussed in the main text, we model the quantum dot junction as a single Anderson impurity coupled to two superconducting leads. The Hamiltonian of the model takes the form

$$H = H_{\rm dot} + H_{\rm leads} + H_{\rm T}. \tag{S1}$$

The first term describes a single-level quantum dot,

$$H_{\rm dot} = \sum_{\sigma=\uparrow,\downarrow} \epsilon_\sigma d_\sigma^\dagger d_\sigma + U n_\uparrow n_\downarrow \,. \tag{S2}$$

Here, $\epsilon_{\uparrow,\downarrow} = \epsilon \pm E_{\rm Z}/2$ gives the single-particle energies: ϵ is the dot energy level measured with respect to the Fermi level in the leads, and $E_{\rm Z} = g\mu_{\rm B}B$ is the Zeeman energy. In the latter, g is the effective g-factor of the level, $\mu_{\rm B}$ is the Bohr magneton, and B is the magnetic field strength. Finally, $U > 0$ is the repulsive Coulomb interaction between the electrons, which disfavors the double occupancy of the impurity, while $n_\sigma = d_\sigma^\dagger d_\sigma$ are number operators for the dot level, with d_σ ($d_\sigma^\dagger$) the electron annihilation (creation) operators.

The many-particle energy levels of Eq. (S2) are divided in two sectors, corresponding to their fermion parity, or equivalently, to their total spin S. The singlet sector includes the states of even parity, which have $S = 0$: the empty state $|0\rangle$ and the pair state $|2\rangle = d_\uparrow^\dagger d_\downarrow^\dagger |0\rangle$. The doublet sector includes the states of odd parity, which have $S = 1/2$: $|\uparrow\rangle = d_\uparrow^\dagger |0\rangle$ and $|\downarrow\rangle = d_\downarrow^\dagger |0\rangle$. It is convenient to introduce the energy $\xi = \epsilon + U/2$, corresponding to half of the energy gap in the singlet sector, so that $\xi = 0$ corresponds to the electron-hole symmetry point, where $|0\rangle$ and $|2\rangle$ are degenerate in energy. The ground state of $H_{\rm dot}$ belongs to the doublet sector for $|\xi/U| < 1/2$.

The second term in Eq. (S1) describes two superconducting reservoirs,

$$H_{\rm leads} = \sum_{i,k} \epsilon_k n_{i,k} + \sum_{i,k} \left(\Delta e^{-i\phi_i} c_{i,k\uparrow}^\dagger c_{i,k\downarrow}^\dagger + \text{h.c.} \right) \tag{S3}$$

where $i = \text{L}, \text{R}$ labels the left and right leads, k labels spin-degenerate single-particle states, $\Delta e^{-i\phi_i}$ is the s-wave pairing potential in each reservoir, and $c_{i,k\sigma}$ ($c_{i,k\sigma}^\dagger$) are the electron annihilation (creation) operators in the leads. The gauge-invariant phase difference between them is $\phi = \phi_{\rm L} - \phi_{\rm R}$. We assume the reservoirs to have identical gap Δ and density of states ρ; this assumption should be reasonable since in the experiment the two leads are made out of a single hybrid nanowire. We further take the g-factor of the reservoirs to be zero, capturing the magnetic field dependence of the combined system in the effective quantum dot g-factor of Eq. (S2).

Finally, the third term is the tunneling Hamiltonian coupling the dot and the reservoirs,

$$H_{\rm T} = \sum_{i,k,\sigma} \left(t_i c_{i,k,\sigma}^\dagger d_\sigma + \text{h.c.} \right) , \tag{S4}$$

where t_i are the dot-reservoir tunnel coupling strengths, which, for simplicity, we choose to be independent of k and spin. The tunneling rate across each barrier is given by $\Gamma_i = \pi\rho\,|t_i|^2$. The tunneling terms in $H_{\rm T}$ break the conservation of the parity and spin in the quantum dot. Nevertheless, the notion of singlet and doublet sectors introduced for the dot Hamiltonian of Eq. (S2) is inherited by the total Hamiltonian of Eq. (S1), provided that the spin S is now regarded as the total spin of the system, including that of quasi-particles in the reservoirs. The same holds for parity, which must be redefined as the parity of the total number of electrons in the system.

Over the years, the model of Eq. (S1) (or immediate extensions of it) has become paradigmatic to describe quantum dots coupled to superconducting leads. It has been studied in different limits and using a variety of numerical methods, often requiring advanced many-body methods such as the numerical renormalization group (NRG) and quantum Monte Carlo for full quantitative descriptions [1]. In the present work, we used NRG methods to extract the energies of the singlet and doublet states for any combination of the model parameters. These energies are then incorporated in a DC SQUID transmon Hamiltonian which is used to match the experimental data and extract estimates of the model parameters. These procedures are detailed in the remainder of this Section.

B. NRG calculation

The NRG method is an iterative procedure for solving quantum impurity problems involving a localized few-level system coupled to a continuum of itinerant electrons (fermionic bath, normal-state or mean-field BCS superconductor).

It consists of several steps: 1) discretization of the continuum parts of the Hamiltonian using a geometric-progression mesh with an accumulation point at the Fermi level (the so-called logarithmic discretization), 2) unitary transformation of the resulting discretized Hamiltonian from the star-geometry (impurity coupling to each representative mesh point) to a linear tight-binding chain representation (the so-called Wilson chain), 3) iterative diagonalization in which the Wilson chain sites are taken into account consecutively [2–6]. The discretization is controlled by the discretization parameter $\Lambda > 1$ which controls the coarseness of the grid. When the discretization is coarse, the results can be improved by twist averaging, which consists of performing the same calculation for several different discretization grids and averaging the results [6, 7]. The growth of the Hilbert space is controlled by the truncation parameters which control the number of states retained after each step of the iteration.

The calculations in this work have been performed with the NRG Ljubljana code [8]. Since the main quantities of interest are the ground state energies in each spin sector, very high quality results can be obtained even with coarse discretization ($\Lambda = 8$) and keeping no more than 3000 states (spin multiplets) in the truncation. We have verified that the twist averaging is not required. The BCS gap was chosen to be $\Delta = 0.1D$, where D is the half-bandwidth. The calculations were performed for a problem with symmetric hybridisations, $\Gamma_\mathrm{L} = \Gamma_\mathrm{R}$. This is sufficient, because the results for an arbitrary coupling asymmetry can be obtained from the following mapping [9]:

$$\phi_S(\phi, a) = 2 \arccos \sqrt{1 - \frac{4a}{(a+1)^2} \sin^2(\phi/2)}, \tag{S5}$$

where $a = \Gamma_\mathrm{L}/\Gamma_\mathrm{R}$ is the asymmetry, ϕ is the BCS phase difference in the asymmetric problem, and ϕ_S is the effective BCS phase difference in the effective symmetric problem.

Such calculations were performed for a set of values of the interaction strength U (from very low values $U = 0.1\Delta$ that correspond to ABS-like subgap states, up to $U = 30\Delta$ that correspond to YSR-like subgap states). In every value of U, a grid of ξ and Γ parameters was set up, and a sweep of ϕ between 0 and π (50 points) has been performed for each (ξ, Γ) pair. The ground state energies are obtained as the sum of all energy shifts [3] performed during the NRG evolution, which has been shown to produce extremely accurate results [7]. Some calculations have also been performed in the presence of a small Zeeman splitting. The results have been collected, documented, and made available on a public repository [10]. The full set of input files and scripts is provided for running the calculations for different parameters or for different Hamiltonians.

Having developed the NRG calculation, we can gain insight into the expected boundaries between singlet and doublet occupation. In Fig. S1(a), we show the phase diagram for the symmetric configuration $\Gamma_\mathrm{L} = \Gamma_\mathrm{R}$ at fixed $\phi = 0$ and $U/\Delta = 5$. In the (ξ, Γ) plane, the phase diagram takes a dome-like shape with the transition value of Γ being the highest at the electron-hole symmetry point $\xi = 0$. At this point, the transition value of Γ diverges if the phase difference between the reservoirs is changed to $\phi = \pi$, because in this case a destructive interference between tunneling events to the left or right occurs. This causes the "dome" in the (ξ, Γ) plane to turn into the "chimney" shown in Fig. S1(b).

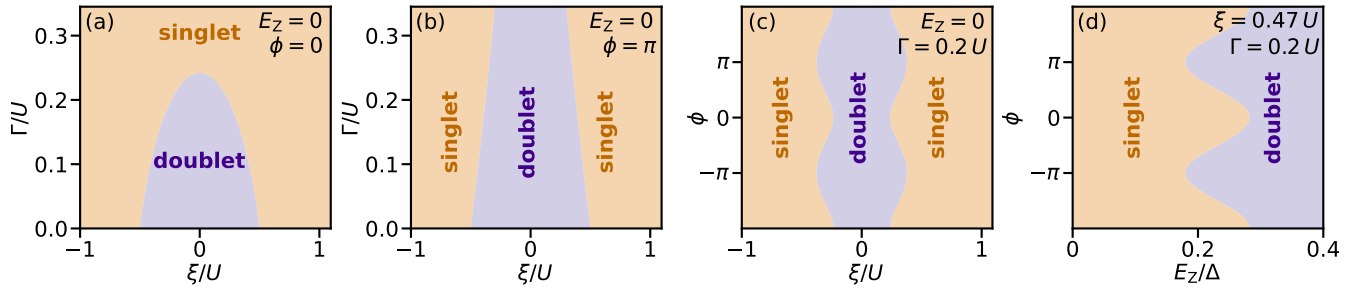

Figure S1. **Boundaries between singlet and doublet ground states extracted from NRG calculations.** (a) Boundary in the $\xi - \Gamma$ plane at $\phi = 0$ for $\Gamma_\mathrm{L} = \Gamma_\mathrm{R}$. (b) Same as (a) for $\phi = \pi$. (c) Boundary in the $\xi - \phi$ plane at $\Gamma = 0.2\,\mathrm{U}$. (d) Boundary in the $E_\mathrm{Z} - \phi$ plane for $\xi = 0.47\,\mathrm{U}$. All panels are for $U/\Delta = 5$.

As mentioned above, at $\Gamma = 0$ the ground state is in the doublet sector for $|\xi/U| < 1/2$. Upon increasing Γ, the Kondo coupling favours the binding of a Bogoliubov quasiparticle in the superconductor to the impurity local moment ("Yu-Shiba-Rusinov" screening), ultimately determining the transition to a singlet ground state at a value Γ_c. The value of Γ_c depends on ξ, ϕ, U and Δ, as well as on the asymmetry between Γ_L and Γ_R. This implies that the singlet-doublet transition can be observed varying any of these parameters individually. Since in the experiment the values of U and Δ are fixed, being determined by the materials and the geometry of the physical device, we focus here on variations in ξ, ϕ, Γ_L and Γ_R.

In Fig. S1(c), we show the singlet-doublet transition boundary in the $\xi-\phi$ plane. The interference effect is modulated continuously by the value of the phase difference ϕ, resulting in periodic oscillations of the boundary. The average position of the oscillating boundary is determined by Γ. In Fig. S1(d), we show the effect of a Zeeman energy E_{Z} in the case when the ground state is singlet at $B = 0$. As mentioned in the main text, a singlet-doublet transition is induced at finite E_{Z} due to the spin-splitting of energy levels in the doublet sector.

C. Transmon diagonalization

Having established how to calculate singlet and doublet potentials using the NRG method, we now turn to their inclusion in the Hamiltonian of the transmon circuit (main text Eq. (1)). To numerically solve the Hamiltonian for an arbitrary potential term $V(\phi)$ we make use of the Fourier decomposition (note that the potential can include an external flux ϕ_{ext}):

$$V(\phi) = E_{\mathrm{J},0} + \sum_n E^{\cos}_{\mathrm{J},n} \cos(n\phi) + \sum_n E^{\sin}_{\mathrm{J},n} \sin(n\phi) \tag{S6}$$

with the components

$$E_{\mathrm{J},0} = \frac{1}{2\pi}\int_{-\pi}^{\pi} V(\phi) d\phi \tag{S7a}$$

$$E^{\cos}_{\mathrm{J},n} = \frac{1}{\pi}\int_{-\pi}^{\pi} V(\phi)\cos(n\phi) d\phi \tag{S7b}$$

$$E^{\sin}_{\mathrm{J},n} = \frac{1}{\pi}\int_{-\pi}^{\pi} V(\phi)\sin(n\phi) d\phi \tag{S7c}$$

where we assume the potential to be a real-valued 2π-periodic function. We can then express the full Hamiltonian in the charge basis as

$$H = 4E_c\hat{N}^2 + E_{\mathrm{J},0} + \sum_n \tfrac{1}{2} E_{\mathrm{J},n}\hat{N}^n_+ + \mathrm{h.c.} \tag{S8}$$

with $E_{\mathrm{J},n} = E^{\cos}_{\mathrm{J},n} - iE^{\sin}_{\mathrm{J},n}$, $\hat{N}$ the charge operator and $\hat{N}^n_+ |N\rangle = |N+n\rangle$.

Upon substituting the potential of main text Eq. (2) into Eq. (S8) and diagonalizing the Hamiltonian, we find the eigenvalues and obtain the energy levels of the combined reference junction and quantum dot junction system. Their difference then results in the transmon's transition frequencies. To numerically compute the eigenvalues we truncate the number of charge states and Fourier coefficients to $N = 35$ for all calculations [11]. We verify that this leads to good convergence for the eigenvalues. We further note that while the presence of the potential offset $E_{\mathrm{J},0}$ does not affect the transmon transition frequencies, its inclusion is crucial: it plays a large role in determining whether the ground state of the combined system corresponds to singlet or doublet occupation for a given set of quantum dot junction parameters.

D. Parameter matching routine

To match the numerical model to the experimental data we have to overcome several complications. First, the mapping between experimental control parameters and those present in the model is not always trivial. As discussed in the main text, V_{p} appears to not only tune ξ but also $\Gamma_{\mathrm{L,R}}$. In turn V_{t} is constructed in such a way that (to first approximation) it does not tune ξ, but it does act on both tunnel rates simultaneously with different, unknown lever arms. For mapping the magnetic field axis to the Zeeman energy the challenge lies in determination of the effective g-factor of the quantum dot, known to be a strongly gate and angle-dependent quantity [12]. Only the flux axis allows for a simpler identification, in particular if one assumes that in the singlet configuration the combined DC SQUID Josephson potential takes its minimal (maximal) values at 0 (π), which should hold for even modest SQUID asymmetry. A separate challenge comes from the large number of parameters of the model: Δ, U, ξ, Γ_{L}, Γ_{R}, and ϕ_{ext}. With 6 potentially correlated parameters to match one has to carefully assess whether the fit is under-determined.

Given these considerations, we identify a specific gate point in the experimental data that could result in a well-constrained situation: the top of the dome shape of Fig. 5(a) in the main text. Here we have access to three measured quantities at a known flux ϕ_{ext}: the singlet and doublet qubit frequencies $f^{\mathrm{s}}_{01}(0)$ and $f^{\mathrm{d}}_{01}(0)$ measured at the boundary

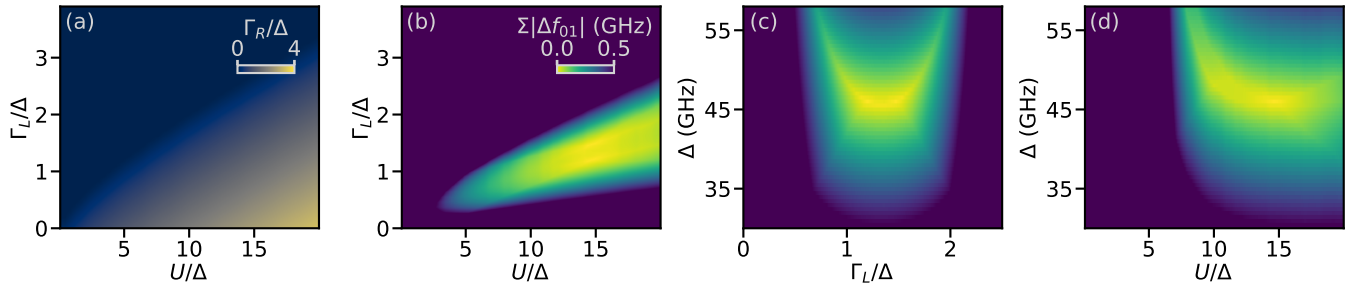

Figure S2. **Numerical matching of model parameters** (a) Calculation of the value of Γ_R that leads to a singlet-doublet transition with other model parameters held fixed. Here we fix $\phi_\mathrm{ext} = 0$ and $\xi = 0$. A value of zero indicates that no such transition occurs. (b) Calculation Eq. (S9) in the $U - \Gamma_\mathrm{L}$ plane evaluated at $\Delta = 46\,\mathrm{GHz}$. (c) Same as (b) in the $\Delta - \Gamma_\mathrm{L}$ plane for $U/\Delta = 12.2$. (d) Same as (b) in the $U - \Delta$ plane for $\Gamma_\mathrm{L}/\Delta = 1.19$.

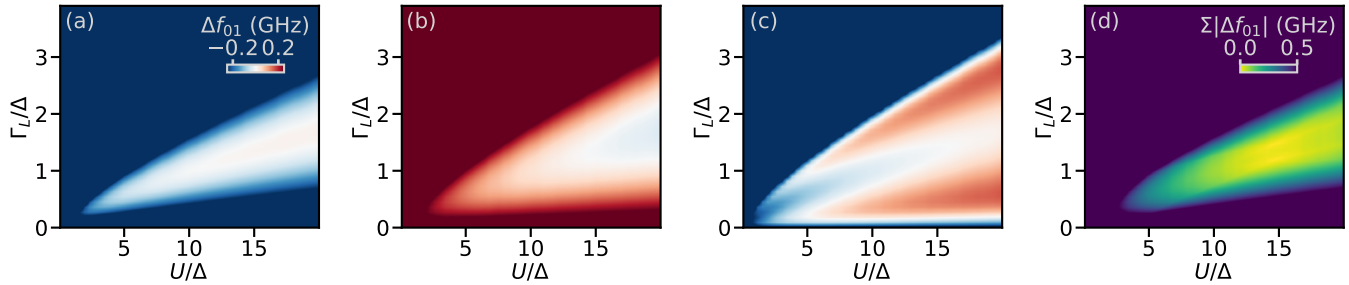

Figure S3. **Numerical matching in $\Gamma_\mathrm{L} - U$ plane** (a) Difference in the calculated and measured singlet qubit frequency at $\phi_\mathrm{ext} = 0$ evaluated at $\Delta = 46\,\mathrm{GHz}$. (b) Same as (a) for the doublet qubit frequency at $\phi_\mathrm{ext} = 0$. (c) Same as (a) for the doublet qubit frequency at $\phi_\mathrm{ext} = \pi$. (d) The absolute sum of the differences in panels (a-c).

of the transition, and also the doublet qubit frequency $f_{01}^\mathrm{d}(\pi)$. We furthermore know that here $E_\mathrm{s} \approx E_\mathrm{d}$ for $\phi_\mathrm{ext} = 0$, since the data lies on the boundary of a singlet-doublet transition versus tunnel gate. Finally, based on the symmetry of the dome shape we identify that this V_P should correspond to $\xi \approx 0$. We can therefore eliminate two of the model parameters (ξ and ϕ_ext) and are left to determine Δ, U, Γ_L and Γ_R.

In a first step we tackle the condition of a singlet-doublet transition occurring versus tunnel gate. For each value of Δ, U and Γ_L we numerically diagonalize the Hamiltonian of Eq. (S8) to determine the lowest energy level of the total circuit for both the singlet and doublet states and find the value of Γ_R for which these energies are equal. For this we use a reference junction potential $V_\mathrm{j} = E_\mathrm{J}(1 - \cos\phi)$ with $E_\mathrm{J} = 12.8$ GHz and $E_\mathrm{c}/h = 210\,\mathrm{MHz}$ as determined in Sec. III. Shown in Fig. S2(a), this results in a U-dependent range of Γ_L for which there is indeed a value of Γ_R that leads to a singlet-doublet transition. Outside of this range Γ_L is so large that the ground state is always a singlet.

Having determined these possible values of Γ_R we calculate the three relevant transmon frequencies $f_{01}^\mathrm{s}(0)$, $f_{01}^\mathrm{d}(0)$, and $f_{01}^\mathrm{d}(\pi)$. These are then compared to the measured values, and an optimal solution is sought that minimizes the sum of the absolute difference between calculation and measurement of all three quantities

$$\Sigma|\Delta f_{01}| = |f_{01}^{\mathrm{s,exp.}}(0) - f_{01}^{\mathrm{s,calc.}}(0)| + |f_{01}^{\mathrm{d,exp.}}(0) - f_{01}^{\mathrm{d,calc.}}(0)| + |f_{01}^{\mathrm{d,exp.}}(\pi) - f_{01}^{\mathrm{d,calc.}}(\pi)|. \tag{S9}$$

In Figs. S2(b-d) we plot a sample of this three-dimensional optimization, while Fig. S3 shows how each panel is constructed from the individual singlet and doublet qubit frequencies. Other than the trivial symmetry between $\Gamma_\mathrm{L,R}$, it appears that there is indeed a single region of parameters matching our data. At its global minimum we find $\Delta/h = 46\,\mathrm{GHz}$ (190 μeV), $U = 12.2\Delta$, $\Gamma_\mathrm{L} = 1.19\Delta$ and $\Gamma_\mathrm{R} = 1.47\Delta$, which results in a precise match to the measured qubit frequencies.

Having determined Δ, U, Γ_L, and Γ_R at this single point in gate space, we attempt to match the model to the V_T axis of the data. To do so we fix Δ and U to the determined values and for each value of V_T find the best set of $\Gamma_\mathrm{L,R}$ to match the data. To determine these two parameters we have two measured quantities: up to the transition we have $f_{01}^\mathrm{d}(0)$ and $f_{01}^\mathrm{d}(\pi)$, and after the transition we have $f_{01}^\mathrm{s}(0)$ and $f_{01}^\mathrm{d}(\pi)$. This procedure results in good correspondence to the experimental results, as shown in main text Fig. 5(c,d). We note that by construction this captures all the granularity and measurement uncertainty of the experimental data, even though the underlying quantities might have been more smooth. A subsequent procedure that attempts to match V_P to ξ did not turn out to be unique, as V_P appears to also act on $\Gamma_\mathrm{L,R}$. We therefore leave this mapping undetermined.

The uncertainty in the extracted quantities is affected by several factors. The first is the measurement accuracy; we measure the qubit frequency with MHz-scale precision. Based on numerical evaluation of the model, this precision in qubit frequency should limit the extracted parameter accuracy to several GHz. A more substantial uncertainty comes from the determination of the transmon island charging energy E_c, which is typically determined from the transmon transition anharmonicity $\alpha = f_{12} - f_{01}$. While the anharmonicity can be measured to high precision, a complication arises from the usage of a nanowire based Josephson junction as the reference junction. Up to now we have assumed its potential to take the form $V(\delta) = E_J(1-\cos\delta)$; that of a conventional superconductor-insulator-superconductor (SIS) tunnel junction governed by many weakly transparent channels. In this case we find that $E_c/h = 210\,\mathrm{MHz}$, resulting in the parameter estimates given above. However, previous work has found that nanowire-based Josephson junctions are better described by several or even a single transport channel, such that $V(\delta) = -\sum_n \Delta\sqrt{1 - T_n \sin^2\delta/2}$. This change in potential shape can lead to a strong reduction in the anharmonicity, and thus an underestimation of E_c when using the SIS potential [13]. We therefore also match our reference junction dependence to a single transport channel, which is the most extreme case for a reduction in the anharmonicity, finding good agreement with a single transport channel of $T = 0.58$. This in turn leads to an extracted $E_c/h = 306\,\mathrm{MHz}$ (see Sec. III), resulting in a different set of extracted quantum dot parameters. In particular, we now find $\Delta = 30.5\,\mathrm{GHz}$ and $U = 17.3\Delta$. This value of the induced gap in the InAs-Al nanowire is on the low end of what is typically found in DC transport experiments, which might hint at a reduced proximity effect in the ungated leads [14, 15].

Capacitance simulations of the full circuit do not provide an unambiguous answer for which of the two limits is more appropriate, as the circuit was designed to target $E_c/h = 250\,\mathrm{MHz}$ which falls in the center of the estimated range. As it stands we therefore do not have to uniquely determine the experimentally realized E_c and thereby resolve the uncertainty in the extracted quantities. However, future works could make use of additional circuit QED compatible quantum dot probes such as direct DC access [16] or dispersive gate-sensing techniques [17] to independently characterize several model parameters and further constrain the matching.

E. Calculated 2D maps

Having established how to match the model parameters to the data, we now turn to the reconstruction of the full 2D dependencies measured in the experiment (Fig. S4). For the plunger versus tunnel gate dependence, we calculate both the singlet and doublet qubit frequencies for all values of $\Gamma_{L,R}$ encoded by V_T for a range of ξ at both $\phi_{ext} = 0$ and π. We subsequently mask the data according to the ground state of the combined transmon Hamiltonian, and obtain a result that closely approximates the measured data (main text Fig. 5). Using the same set of quantum dot junction parameters, we also perform a similar procedure for the 2D map of plunger gate and external flux, resulting good correspondence with main text Fig. 4.

F. State population

We now turn to the singlet and doublet lifetimes determined in device B. For this device we could not identify a measurement point where a unique set of parameters matched the measured data, and can therefore not make a quantitative comparison to the numerics. Instead, we attempt to gain some intuition about the obtained results based on the parameters of device A.

In main text Fig. 7 we extract $\log_{10}(T_d/T_s)$, the ratio of the lifetimes of singlet and doublet occupation. If the system was in thermal equilibrium with a bath of temperature T, one would naively expect that the relative lifetimes should follow the state populations $P_{s,d}$ as described by a Maxwell-Boltzmann distribution:

$$P_i = \frac{1}{Z} g_i \exp\left(-E_i/k_B T\right) \tag{S10}$$

where g_i is the degeneracy of the state, $E_{s,d}$ are the singlet and doublet energies, and k_B is the Boltzmann constant. We take $Z = 2\exp\left(-E_d/k_B T\right) + \exp\left(-E_s/k_B T\right)$, where we neglect potential other many-body states which should be unoccupied at the experimentally relevant temperatures. In Fig. S5(a) we then plot $\log_{10}(P_d/P_s)$, choosing a bath temperature of 400 mK. Qualitatively this follows the same trend as observed experimentally, with a sharp boundary at the phase transition and a saturated population imbalance away from that. We stress once-more that this is not a quantitative comparison. However, the need for a temperature far in excess of the refrigerator's base temperature of 20 mK could hint at a non-thermal origin such as non-equilibrium quasiparticles [18].

In the main text we also speculate that non-thermal effects lie at the origin of the experimentally observed contours of fixed lifetime ratio's. We corroborate this in Fig. S5(b), where we plot the energy difference between singlet and

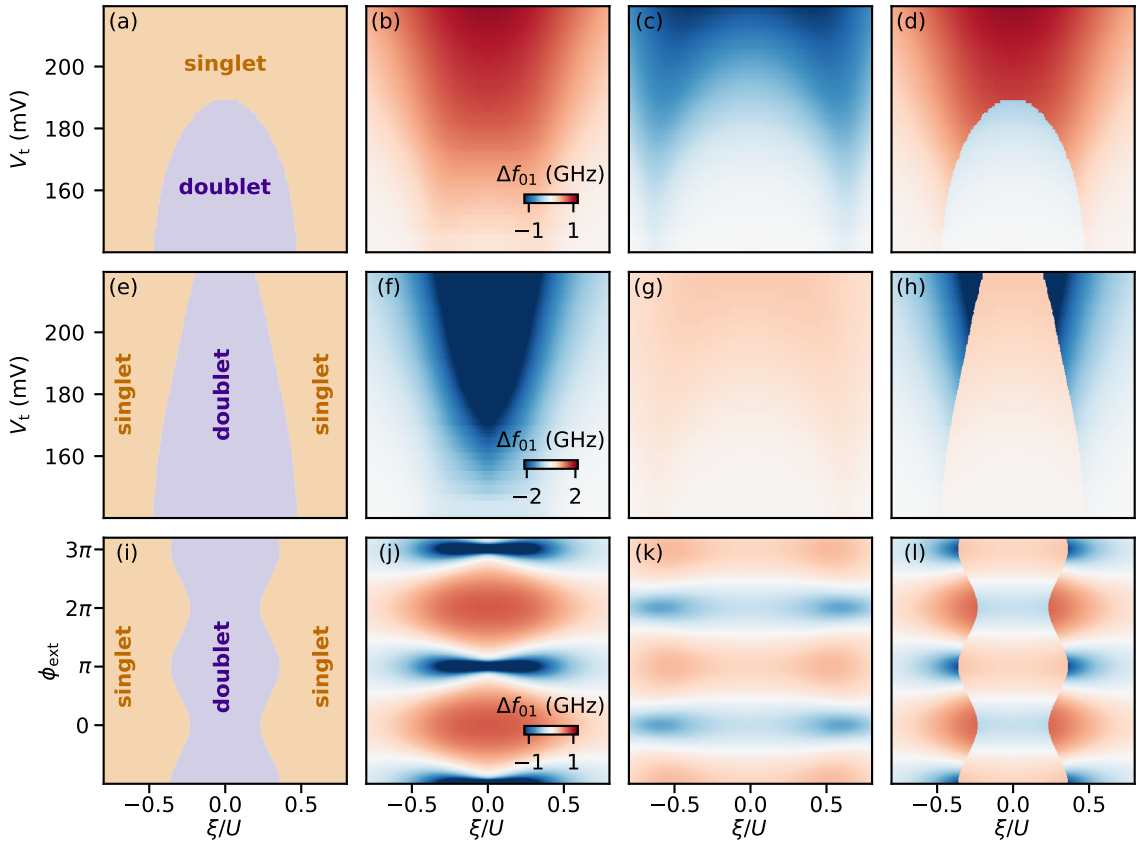

Figure S4. **Numerically calculated transmon frequency maps** (a,e,i) Boundaries between singlet and doublet ground states extracted from NRG calculations for $\phi_{ext} = 0$, $\phi_{ext} = \pi$, and $\Gamma_R = 1.23\Gamma_L$ respectively. Panels (b-d), (f-h), (j-l) show how the singlet qubit frequency, the doublet qubit frequency, and the combined result conditioned on the ground state of panels (a,e,i) respectively depend on the parameters. Each row shares the same color map. This leads to saturation of the color map in the panels corresponding to the unconditioned singlet and doublet qubit frequencies, but facilitates comparison to the experimental results. For all panels $U/\Delta = 12.2$ and $\Delta = 46\,\mathrm{GHz}$.

doublet occupation of the quantum dot junction. This quantity exhibits distinct contours of equal energy difference that qualitatively match those found in the experiment. If the environment has spectral components resonant with these specific energies, one could expect these to modify the dynamics.

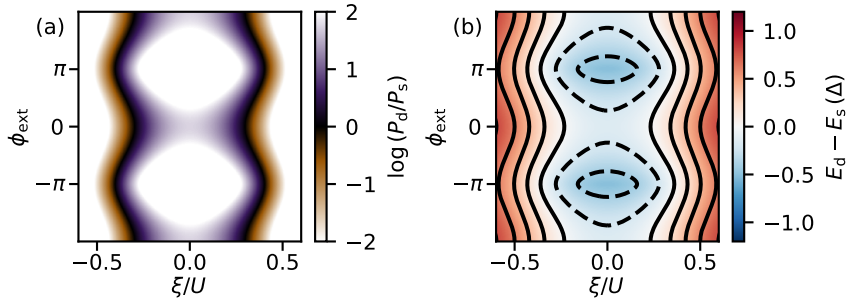

Figure S5. **State population versus ξ and ϕ_{ext}** (a) Ratio of the expected state population as calculated from Eq. (S10) for a temperature of 400 mK. The colormap is saturated to facilitate comparison to main text Fig. 7. (b) Difference between doublet and singlet energy. Each contour indicates a boundary of equal energy difference. Parameters are the same as that of Fig. S4.

II. DEVICE AND EXPERIMENTAL SETUP

A. Nanofabrication details

The device fabrication occurs in several steps using standard nanofabrication techniques, and it is identical for device A and B. The substrate consists of 525 µm-thick high-resistivity silicon, covered in 100 nm of low pressure chemical vapor deposited Si_3N_4. On top of this a 20 nm thick NbTiN film is sputtered, into which the gate electrodes and circuit elements are patterned using an electron-beam lithography mask and SF_6/O_2 reactive ion etching. Subsequently, 30 nm of Si_3N_4 dielectric is deposited on top of the gate electrodes using plasma enhanced chemical vapor deposition and then etched with buffered oxide etchant. The nanowire is then deterministically placed on top of the dielectric using a nanomanipulator and an optical microscope. For this we use an approximately 10 um-long vapour-liquid-solid (VLS) hexagonal InAs nanowire with a diameter of 100 nm and a 6 nm-thick epitaxial Al shell covering two facets [19]. After placement, two sections of the aluminium shell are removed by wet etching with MF-321 developer. These sections form the quantum dot junction and the reference junction, with lengths 200 nm and 110 nm respectively. A zoom-in of the the quantum dot junction is shown in Fig. 2(d) of the main text. The reference junction is controlled by a single 110 nm-wide electrostatic gate, set at a DC voltage V_J. The quantum dot junction is defined by three 40 nm-wide gates separated from each other by 40 nm, set at DC voltages V_L, V_C and V_R. Note that in Fig. 2(d) the gates appear wider (and the gaps between gates appear smaller) than stated due to distortion by the Si_3N_4 layer; the given dimensions are therefore determined from a scanning electron microscopy image taken before the deposition of the dielectric. After the junction etch the nanowire is contacted to the transmon island and to ground by an argon milling step followed by the deposition of 150 nm-thick sputtered NbTiN. Finally, the chip is diced into 2 by 7 millimeters, glued onto a solid copper block with silver epoxy, and connected to a custom-made printed circuit board using aluminium wirebonds.

B. General chip overview

Optical microscope images of the chips containing devices A and B are shown in Figs. S6(a) and (b), respectively. Each chip, 7 mm long and 2 mm wide, consists of four devices coupled to the same transmission line. For the chip containing device A, only one device was functional. Out of the other three, one did not have a nanowire, another contained three nanowires stuck together, and for the third device a gate electrode showed no response. The chip of device B includes an on-chip capacitor on the input port of the transmission line to increase the signal-to-noise ratio. For this chip only two of the devices were bonded: device B, which was functional, and another device that did not show any response to the electrostatic gates. The two unbonded devices were dismissed based on prior optical inspection, containing two and no nanowires respectively.

C. Flux control with in-plane magnetic field

In all measurements we control the external flux ϕ_ext with the in-plane component of the magnetic field perpendicular to the nanowire, B_y, as illustrated in Fig. S7 [20], for which one flux quantum corresponds to 2.2 mT. This is done since flux tuning with the out-of-plane magnetic field B_x led to strong hysteric behaviour in the resonator as well as flux jumps in the SQUID loop. We attribute these effects to Abrikosov vortex generation and the presence of superconducting loops on the chip, causing screening currents.

D. Flux jumps in device A when $|B| < 9\,\mathrm{mT}$

For all measurements of device A, the value of the applied magnetic field is kept above 10 mT to prevent flux jumps observed when $|B| < 9\,\mathrm{mT}$. In particular, for Figs. 3-5 in the main text, $B_z = 10\,\mathrm{mT}$. The reason for this is purely technical. Device A contains various on-chip aluminium wire-bonds connecting separate sections of the ground plane together. Below the critical magnetic field of aluminium ($\sim$10 mT [21]) these wire bonds create superconducting loops close to the device region, and have a significant cross-section perpendicular to the chip plane. In this regime, the application of an in-plane magnetic field B_y generates unwanted currents across these superconducting loops, which in turn result in multiple jumps observed in the flux through the SQUID loop (Fig. S8), making it impossible to reliably control ϕ_ext. Applying a field $|B| > 9\,\mathrm{mT}$ turns the aluminium wire bonds normal and prevents the unwanted flux jumps, as shown in Fig. S8(a). As this magnetic field is small compared to other energy scales involved, it should not

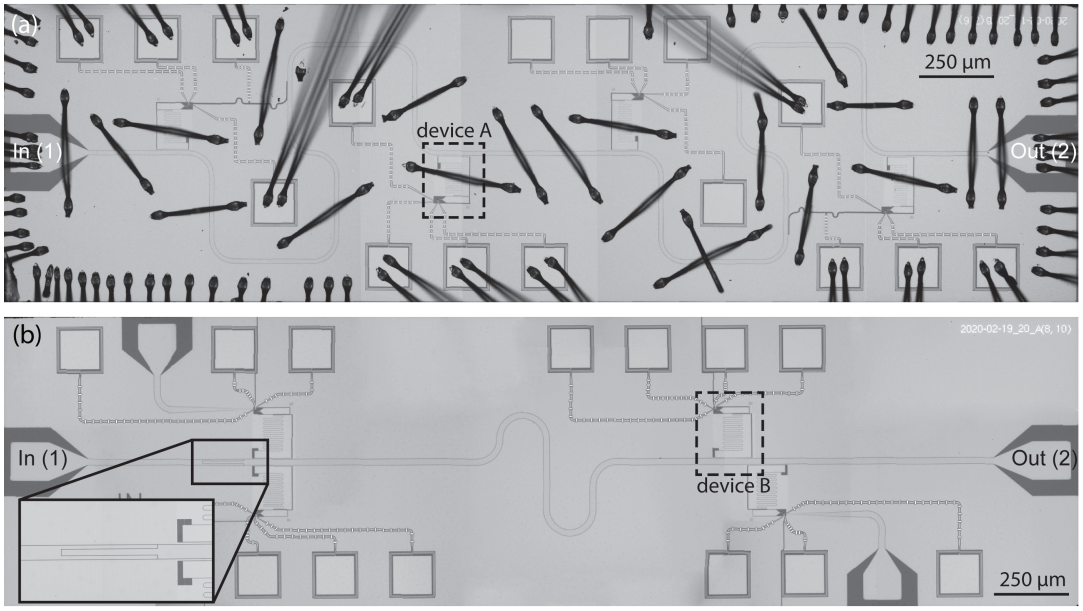

Figure S6. **Chip design.** (a) The chip of device A, containing four nearly identical devices coupled to the same transmission line. The image is taken after wire-bonding onto a PCB. (b) The chip of device B, incorporating an input capacitor in the transmission line (enlarged in inset). The image is taken before wire-bonding onto a PCB.

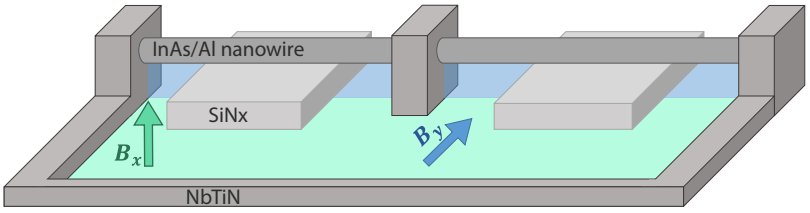

Figure S7. **Flux control with B_y.** The nanowire is elevated with respect to the NbTiN plane due to the gate dielectric. This defines a loop area perpendicular to B_y. B_y can therefore be used to control the flux through the SQUID loop while keeping the out-of-plane field component (B_x) fixed, reducing the occurance of external flux jumps.

affect the physics under study. We further note that the absence of superconducting loops containing wire-bonds in device B made it possible to measure this device at $B_z = 0$ mT without suffering from similar flux jumps.

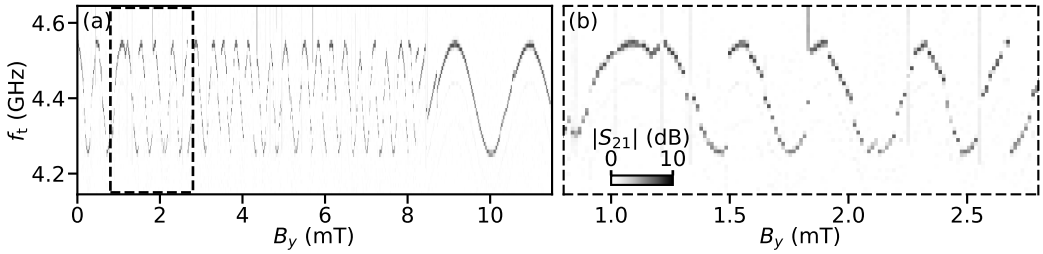

Figure S8. **Flux jumps under $|\mathbf{B}| = 9$ mT for device A.** Multiple flux jumps and a distorted periodicity observed at low magnetic fields disappear when $|B| > 9\,\mathrm{mT}$. Here, $B_z = B_x = 0$

E. Cryogenic and room temperature measurement setup

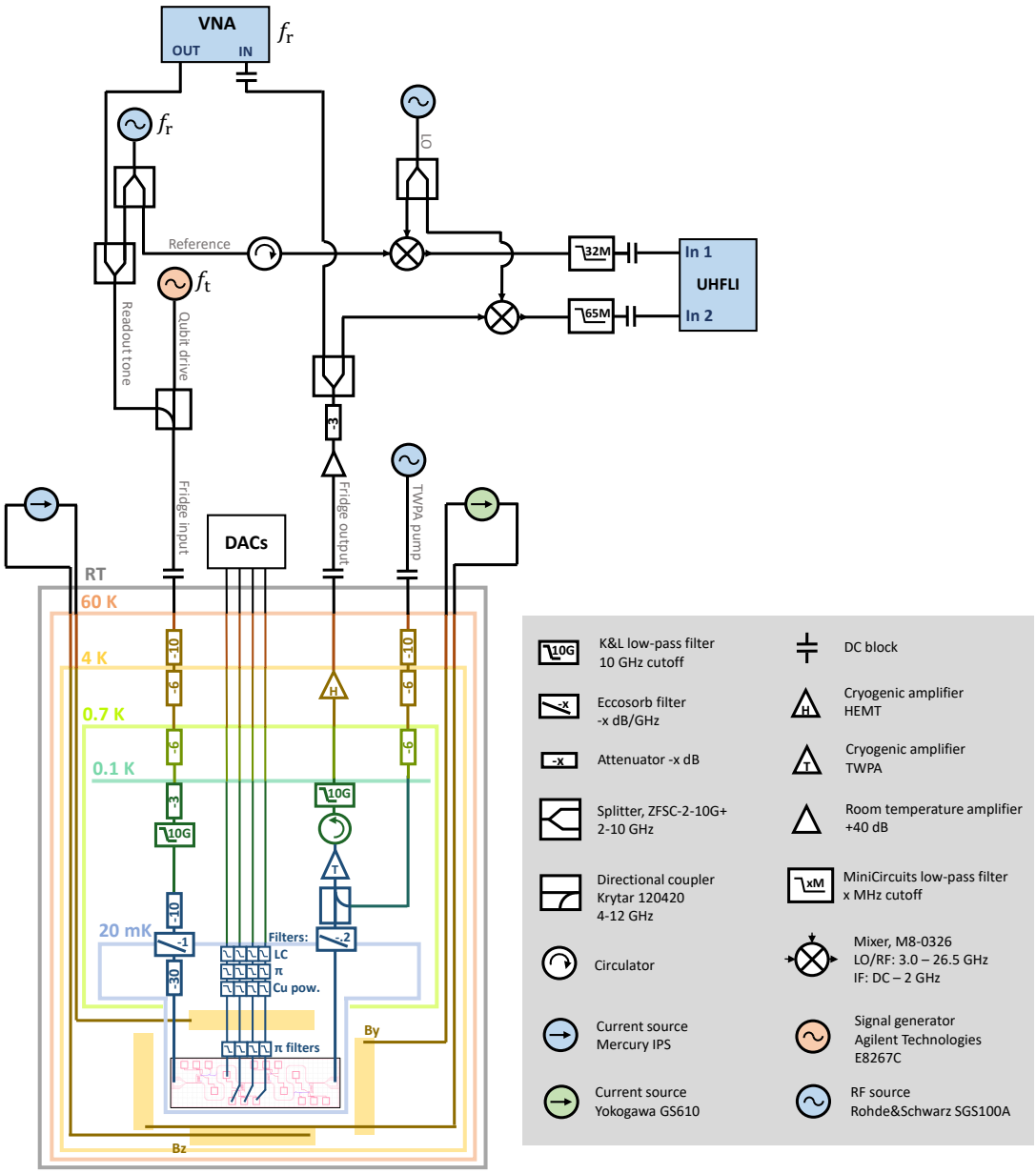

Figure S9. **Measurement setup at cryogenic and room temperatures.** Both devices are measured in the same Triton dilution refrigerator with a base temperature of 20 mK. It contains an input RF line, an output RF line and multiple DC gate lines. The DC gate lines are filtered at base temperature with multiple low-pass filters connected in series. The input RF line contains attenuators and low-pass filters at different temperature stages, as indicated. The output RF line contains a travelling wave parametric amplifier (TWPA) at the 20 mK temperature stage, a high-electron-mobility transistor (HEMT) amplifier at the 4 K stage, and an additional amplifier at room temperature. A three-axis vector magnet (x-axis not shown) is thermally anchored to the 4 K temperature stage, with the device under study mounted at its center. The B_z component of the magnetic field is controlled with a MercuryiPS current source while the B_x and B_y axes are controlled with Yokogawa GS200 and GS610 current sources respectively. At room temperature a vector network analyzer (VNA) is connected to the input and output RF lines for spectroscopy at frequency f_r. On the input line, this signal is then combined with the qubit drive tone at frequency f_t for two-tone spectroscopy. A separate tone at f_r only used for time-domain measurements is also combined onto this line. For time-domain measurements the output signal is additionally split off into a separate branch and down-converted to 25 MHz to be measured with a Zurich Instruments ultra-high frequency lock-in amplifier.

III. BASIC CHARACTERIZATION AND TUNE UP OF DEVICE A

A. Reference junction characterization

In this section we investigate the basic behaviour of the reference junction versus junction gate voltage V_J and magnetic field B_z when the quantum dot junction is completely closed. This information is used to choose a V_J set-point, $V_J = 640\,\text{mV}$, which maintains a good SQUID asymmetry in all regimes of interest. Figs. S10(a) and (b) show the V_J dependencies of the resonator and transmon frequencies, respectively. As V_J is varied, different junction channels open sequentially [22, 23], with transparencies that increase non-monotonically due to mesoscopic fluctuations at the junction. This in turn affects the transmon's E_J and results in the observed fluctuations of its frequency.

The B_z dependencies of f_{01} and $f_{02}/2$ at $V_J = 640\,\text{mV}$ are shown in Fig. S10(e). From this we estimate both the transmon island charging energy E_c (not to be confused with U, the charging energy of the quantum dot junction) and the parameters of reference junction potential used in Sec. I D to match the measurements to the numerical calculations. Illustrated in this figure is a fit of the data with a Josephson potential governed by a single Andreev level at the junction $V(B,\delta) = -\Delta(B)\sqrt{1 - T\sin^2\frac{\delta}{2}}$. Here $\Delta(B) = \Delta\sqrt{1-(B/B_c)^2}$ is the field dependent superconducting gap [21], Δ is the superconducting gap at zero field, B_c is the critical magnetic field and T is the transparency of the junction. As the fit is not constrained well enough to provide a unique solution, we fix $\Delta/h = 60$ GHz based on recent experiments on the same nanowires [24]. We obtain $E_c/h = 306$ MHz, $T = 0.58$, and $B_c = 413$ mT, resulting in an effective $E_J \sim \Delta T/4 = 8.7$ GHz. A similar procedure is then performed for $V_j = E_J(1-\cos\delta)$, resulting in $E_c/h = 210\,\text{MHz}$ and $E_J/h = 12.8$ GHz.

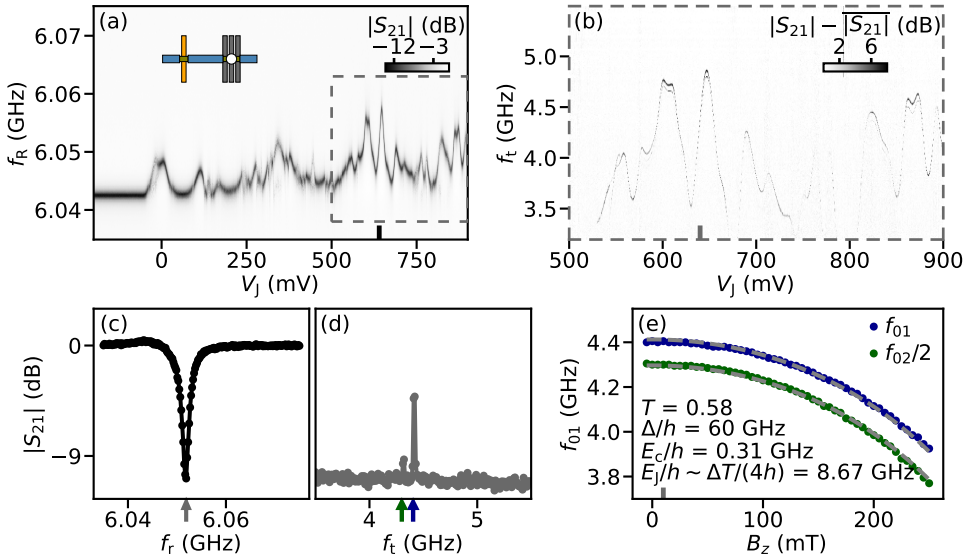

Figure S10. **Reference junction characterization for device A.** (a) V_J dependence of single-tone spectroscopy when the quantum dot junction is pinched-off ($V_C = 52.4\,\text{mV}$, $V_L = 470\,\text{mV}$, $V_R = 373\,\text{mV}$). At low V_J values the reference junction is pinched-off and $E_J \sim 0$, thus the resonator is at its bare resonance frequency. As V_J increases, the resonator frequency increases non-monotonically due to mesoscopic fluctuations of the overall increasing transmission of different junction channels. (b) V_J-dependence of two-tone spectroscopy for the V_J range indicated in (a) with a dashed line rectangle. The black lines in (a) and (b) indicate the $V_J = 640\,\text{mV}$ set-point which sets the transmon frequency to its set-point used for the main text figures, $f_{01} = f_{01}^0 = 4.4\,\text{GHz}$. (c) Line-cut of (a) at the V_J set-point, showing a resonance. (d) Line-cut of (b) at the V_J set-point, showing two peaks. The highest peak, at higher frequency, appears when the second tone frequency matches the transmon frequency ($f_t = f_{01}^0$). The lower peak corresponds to $f_{02}/2$ and shows the anharmonicity of the transmon. For (d), the first tone frequency f_r is fixed at the bottom of the resonance, indicated with a grey arrow in (c). (e) B_z evolution of f_{01}^0 and $f_{02}/2$ at $V_J = 640\,\text{mV}$.

We can use these parameters to estimate the experimentally-realized SQUID asymmetry $\alpha_S = E_J/E_{J,QD}$ where $E_{J,QD}$ denotes the effective quantum dot junction Josephson energy. To do so we estimate $E_{J,QD}$ from the calculated qubit frequencies of the singlet and doublet obtained in Sec. I D through the relation $\hbar\omega_{01} \approx \sqrt{8E_{J,QD}E_c} - E_c$ [11]. We find that $\alpha_S > 10$ for almost all of the parameter range, exceeding 30 for low values of V_t. The asymmetry is at its smallest for the upper values of V_t in the vicinity of $\xi = 0$, where we find a minimum asymmetry $\alpha_S = 4$. We note that the effects of these variations in asymmetry are fully captured by the numerical model; its effects are predominantly

on the modulation of the qubit transition frequency with flux and not on the position of the singlet-doublet transition boundaries.

B. Quantum dot junction characterization

In this section we show the basic behaviour of the quantum dot gates when the reference junction is closed. Fig. S11 shows effective pinch-off curves for all three quantum dot gates ramped together (a) and for each of them separately, when the other two are kept at 1250 mV (b-d). This shows that each of the three quantum dot gates can independently pinch off the quantum dot junction even if the other gates are in the open regime, signifying strong lever arms and good gate alignment. We note that these are not pinch-off curves as encountered in conventional tunnel spectroscopy. They reflect the voltages at which there is no longer a measurable transmon transition frequency mediated by the quantum dot junction, which could either be due to low tunneling rates or a full depletion of the quantum dot.

We further note that the gate setpoint chosen for the measurements shown in the main text should not be directly compared to the individual pinch-off curves shown here. In panels (b-d) the non-varying quantum dot gates are kept fully open at 1250 mV which, due to cross coupling between gates, results in lower pinch-off values than those at the gate setpoint used for the measurements in the main text.

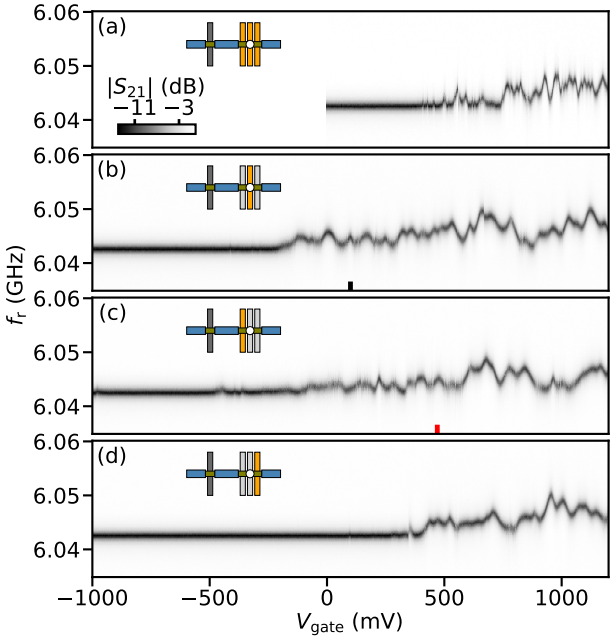

Figure S11. **Quantum dot gates characterization for device A.** (a) Gate voltage dependence ($V_L = V_C = V_R = V_{gate}$) of single-tone spectroscopy, showing how the quantum dot junction is pinched off at V_{gate} values lower than 300 mV. (b-d) V_C, V_L and V_R dependence, respectively of single-tone spectroscopy. In each panel, the two unused gates are kept at 1250 mV. This shows how each of the three quantum dot gates can independently pinch off the quantum dot junction. For all panels, the reference junction is closed ($V_J = -200$ mV). The black line in (b) indicates the value of $V_C = 100$ mV at which Fig. S12 is taken. The red line in (c) indicates the fixed value of $V_L = 470$ mV at which all main text figures are taken.

C. Device tune up

This section describes the process of tuning up the quantum dot gates to the setpoint used for the main text figures. We start by closing the reference junction ($V_J = -200$ mV) and going to a point in quantum dot gate voltages near pinchoff ($V_C = 100$ mV, $V_L = 250$ mV and $V_R = 400$ mV, see Fig. S11). Monitoring the frequency of the resonator while varying one of the gates reveals small shifts away from its bare frequency which resemble the shape expected for quantum dot resonances (Fig. S12(a)). Fixing the readout frequency f_r at the bare frequency of the resonator, one can map out the regions where these shifts happen on a two-dimensional map versus the left and right gates (Fig. S12(b)). In such maps, a pixel with a dark color indicates the resonator is not shifted from its bare frequency while a bright pixel indicates a shift of the resonator frequency, which we can use to identify potential regions of interest.

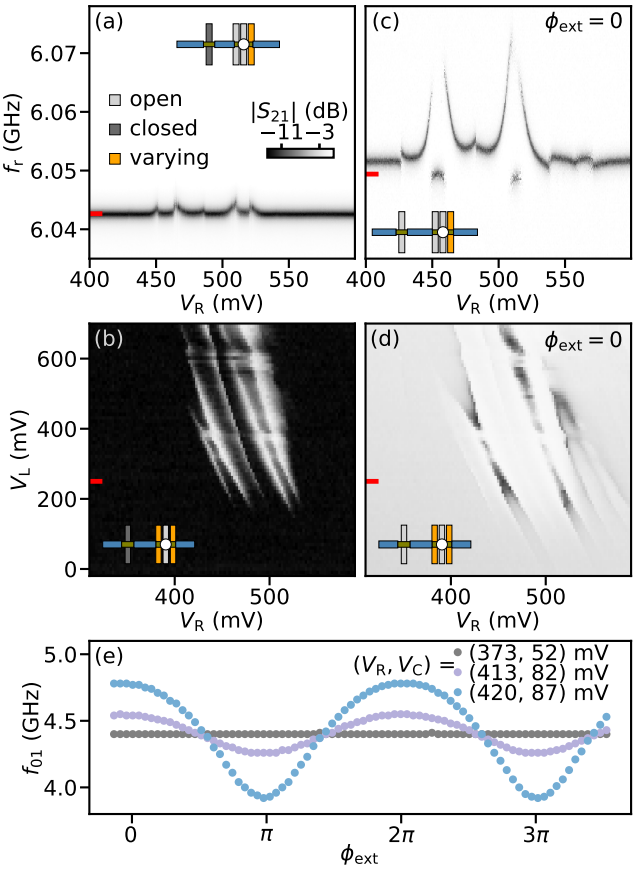

Figure S12. **Quantum dot tune up for device A.** (a) Single-tone spectroscopy measured at V_L = 250 mV, exhibiting two small resonances. Here the reference junction is fully closed (V_J = -200 mV). The red line indicates the readout frequency used in panel (b). (b) Single frequency readout of the resonator. Bright colors indicate a shift in the resonance frequency, marking the onset of supercurrent through the dot. The red line indicates the V_L value of panel (a). (c) Same as panel (a) but with the reference junction opened to the V_J = 640 mV setpoint used throughout the manuscript. The two junctions in parallel form a SQUID, increasing the qubit frequency and in turn the resonance frequency. Measured at $\phi_{ext} = 0$. (d) Same as panel (b) but with the reference junction set to V_J = 640 mV and $\phi_{ext} = 0$, measured at the frequency indicated with a red line in (c). For (a-d), V_C = 100 mV (close to pinchoff), indicated with a black line in Fig. S11. (e) f_{01} versus ϕ_{ext} at fixed V_J = 640 mV, for three quantum dot gates setpoints corresponding to a quantum dot junction which is fully closed (grey), slightly open (violet) or very open (blue) showing the DC SQUID behaviour of the two parallel Josephson junctions.

After identifying such a region in V_L-V_R space, we open the reference junction to its set-point V_J = 640 mV, which lifts the reference transmon frequency to f_{01}^0 = 4.4 GHz, closer to the bare resonator frequency. This magnifies the dispersive shift of the resonator and, furthermore, brings the external flux into the picture. As shown in Fig. S12(e), the asymmetric SQUID behaves as expected for different quantum dot gate setpoints. The reference junction sets the reference value for the transmon frequency, f_{01}^0, and the quantum dot contributes with small variations above or below this setpoint due to constructive or destructive interference, respectively.

Fixing $\phi_{ext} = 0$ and repeating the initial measurement versus V_R with the reference junction open reveals much stronger deviations of the resonant frequency than before (Fig. S12(c)). Importantly, the observed resonant frequency is now discontinuous, which, as detailed in the main text, is a signature of a singlet-doublet transition of the quantum dot junction. We tentatively identify the regions for which the resonator frequency is shifted to lower values as doublet regions and perform single frequency readout versus V_R and V_L, now with f_r fixed at the resonator frequency corresponding to doublet regions (Fig. S12(d)). The resulting two-dimensional map reveals regions for which the transmission amplitude signal is low (dark regions in Fig. S12(d)) which we identify as potential regions with a doublet ground state.

The next step for tuning up is identifying an isolated region where the quantum dot is in a doublet ground state and exploring the behaviour versus the central quantum dot gate. This is shown in Fig. S13. As V_C is varied at $\phi_{ext} = 0$ (Fig. S13(c)), the resonator first shows a displacement towards higher frequencies to then abruptly drop to a lower frequency, to then finally go back to the higher frequencies once-more. As detailed in the main text, we identify this

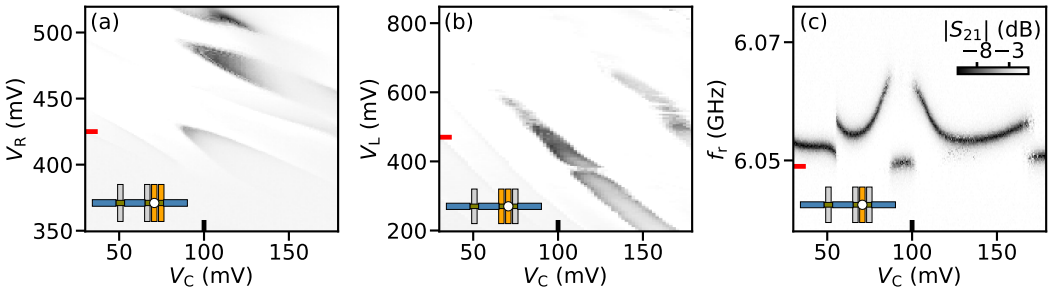

Figure S13. **Quantum dot gate dependence for device A.** (a) Single frequency readout of the resonator at the frequency indicated in Fig. S12(c) with a red line, performed versus V_C and V_R for fixed $V_L = 470\,\mathrm{mV}$. (b) Same as (a) but versus V_C and V_L and for fixed $V_R = 425\,\mathrm{mV}$. (c) Single-tone spectroscopy versus V_C, measured at $V_L = 470\,\mathrm{mV}$ and $V_R = 425\,\mathrm{mV}$, revealing a quantum dot resonance. For all panels $\phi_{ext} = 0$.

behaviour with a singlet-doublet transition as the relative level of the quantum dot ξ is being varied. Figs. S13(a) and (b) show how this central doublet ground state region varies with each of the two lateral quantum dot gates. In both cases we observe a dome shape, resembling the behaviour we would expect when varying the tunnel coupling between quantum dot and leads. However, these dome shapes are rotated in V_C-V_R and V_C-V_L space. This is understood as the result of cross coupling between the different quantum dot gates.

After identifying the cross coupling effect between different quantum dot gates, we define a new set of virtual gates in an attempt to tune the model parameters independently. We fix V_L =470 mV (set-point kept for all results shown in the main text) and focus on V_R-V_C space. Fig. S14(b) shows the dome shape previously identified in V_R-V_C space. We identify a line along the dome (indicated with a dashed line) for which the quantum dot level appears to be fixed and define new plunger virtual gate (V_P, perpendicular to this line) and right tunnel virtual gate (V_T, along this line) (see Fig. S14(d)). This rotated gate frame is the one used for the main text. Note that this routine does not guarantee that V_P does not affect the tunneling rates. It rather ensures that V_T does not (strongly) affect the quantum dot level ξ.

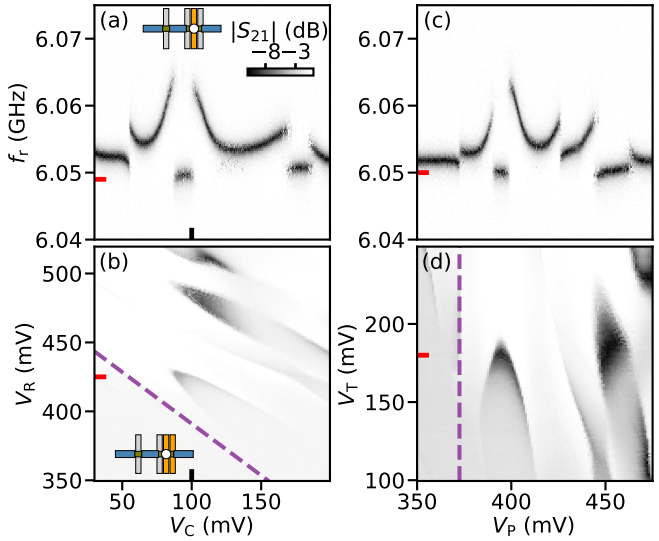

Figure S14. **Gate compensation for device A.** (a) Single-tone spectroscopy versus $V_C$at $V_R = 427\,\mathrm{mV}$. (b) Single frequency readout of the resonator measured versus the central (V_C) and right (V_R) quantum dot gate voltages, performed at a at fixed V_L 470 mV. The red line indicates the V_R value of panel (a). (c) Resonator spectroscopy versus V_P at $V_T = 180\,\mathrm{mV}$. (d) Same as (b) but in the transformed coordinate frame, measured vs. the virtual plunger (V_P) and right tunnel (V_T) gate voltages. In (a) and (c), the red lines indicate the readout frequencies used in panels (b) and (d), respectively. For all panels $\phi_{ext} = 0$.

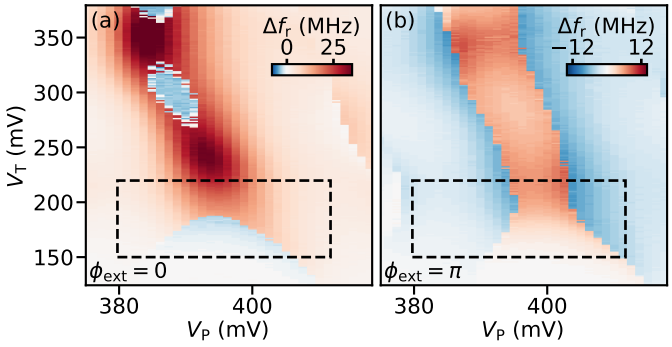

Figure S15. **Extended V_T dependence.** (a) Δf_r versus V_P and V_T at $\phi_{ext} = 0$, revealing singlet (red) and doublet (blue) ground state regions separated by sharp transitions. (b) Same as (a) but for $\phi_{ext} = \pi$. We note that the plunger gate axis is shifted by about 5 mV with respect to (a) and the data shown in the main text, which we speculate is due to an irreproducible gate jump. Dashed rectangles indicate the gate ranges in which the measurements of Fig. 5 of the main text are taken.

D. Larger tunnel voltage range

In Fig. S15 we show the behaviour of the singlet and doublet regions beyond the V_T range investigated in Fig. 5 of the main text. At $\phi_{ext} = \pi$ we do not observe the doublet phase boundary fully closing for any V_T. According to theory, this should only occur if $\xi \approx 0$ and $\Gamma_L \approx \Gamma_R$ are maintained at each gate setting in the experiment. That this condition would remain satisfied for any V_T is implausible given the cross-coupling present in the system. We instead speculate that at higher gate voltages the tunnel rates cease to be a monotonically increasing function, which is substantiated by the tunnel gate dependence at $\phi_{ext} = 0$. Here we observe a temporary recovery of the doublet region at higher V_T, which should not occur for increasing values of Γ. We further speculate that in this regime of increasingly large Γ/U the dot can eventually be tuned to a different charge configuration, involving energy levels not captured by the single-level model of main text Eq. (6).

We note that for these measurements only single tone spectroscopy was performed. We therefore plot $\Delta f_r = f_{res} - f^0_{res}$, where f^0_{res} denotes the resonator frequency with the quantum dot junction pinched off. Its qualitative interpretation is the same as that of Δf_{01} used in the main text.

E. State selective spectroscopy

For the measurements performed close to singlet-doublet transitions, single-tone spectroscopy simultaneously shows two resonances whose relative depth varies with the distance from the transition. This is once more illustrated in Fig. S16, which shows single-tone spectroscopy at several different V_P regions while ϕ_{ext} is varied. It corresponds to the measurements of Fig. 4 of the main text. In panels (a) and (d) we observe only a single resonance; at these plunger gate values the quantum dot junction is sufficiently deep in the singlet and doublet parity sector respectively that only one state is occupied. However, at the plunger gate values between these two regimes (panels (c-d)) the behaviour is more complex. We simultaneously observe two resonances and their depth becomes a function of flux.

For the two-tone spectroscopy measurements in the main text we make use of the averaged occupation of the states captured in the single-tone spectroscopy measurement to identify most occupied state. This can be inferred from the relative depth of the resonances: for example in Fig. S16(e) the most occupied state is the singlet, albeit by a small margin. This in turn allows us to do state selective two-tone spectroscopy, revealing the transmon transition that corresponds to the most occupied state of the system. To do so we fix the frequency of the first tone f_r at the bottom of the deepest resonance, corresponding to the most populated sector of the system. We illustrate this in Figs. S16(f) and (g), where by fixing f_r at the bottom of the resonance corresponding to the singlet (doublet) state we observe a peak only when f_t is equal to the transmon frequency corresponding to the singlet (doublet) state. It is this peak position that we report as f_{01}.

IV. MAGNETIC FIELD DEPENDENCE OF DEVICE A

In this section we elaborate on the analysis of the data shown in Fig. 6(c) in the main text. When varying both ϕ_{ext} and B_z in a measurement, one has to consider the possibility of an unwanted misalignment of the magnetic field

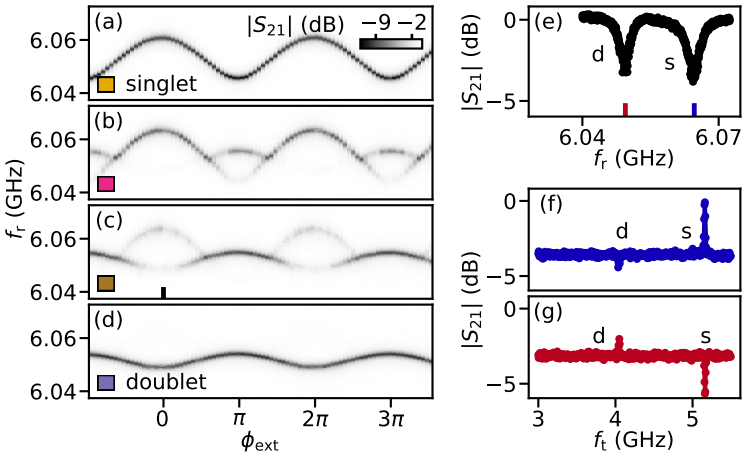

Figure S16. **State selective spectroscopy.** (a-d) ϕ_{ext} dependence of single-tone spectroscopy at four representative V_{P} values, indicated in Fig. 3 in the main text. Traces at intermediate V_{P} values show two resonances simultaneously due to switches on timescales faster than the integration time. (e) Linecut of (c) at $\phi_{\text{ext}} = 0$, indicated by a black line in (c). (f) Two-tone spectroscopy at the same settings as in (e), with the first tone at the frequency of the singlet resonance. The measurement shows a peak at the transmon frequency of the singlet state. (g) Same as (f) but with the readout frequency corresponding to the doublet resonance, which shows a peak at the transmon frequency of the doublet state.

with respect to the nanowire axis. This, in combination with the multiple orders of magnitude difference between the applied B_z (hundreds of mT) and the B_x (less than a μT) or B_y (several mT) needed to thread a flux quantum through the SQUID loop, can result in big changes of the $\phi_{\text{ext}} = 0$ point for different values of B_z. Therefore, one has to re-calibrate the value of B_y that corresponds to $\phi_{\text{ext}} = 0$ for each B_z value. To do so, we use the flux dependence of f_{01} at a gate point for which the quantum dot junction ground state remains a singlet for the whole B_z range as a reference for identifying $\phi_{\text{ext}} = 0$. This gate point is indicated with a grey cross in Fig. S17(a).

The measurement shown in Fig. 6(c) is therefore performed as follows:

for each B_z value **do**
  apply B_z
  for each B_y value **do**
    apply B_y
    measure f_{01} at the grey gate point
    measure f_{01} at the green gate point

For each B_z value we then reconstruct the B_y dependence of ϕ_{ext} through the dependence of the reference gate point (grey). Furthermore, we use this method to identify points in B_y where flux jumps happen and correct for them. While they almost never occur for small magnetic fields, and none of the other data required such a correction, we found that at increasing B_z jumps would occur more often. We believe this is due to a small misalignment between B_z and the plane of the chip. The resulting corrected ϕ_{ext} reference is shown in Fig. S17(b), while Fig. S17(d) shows several linecuts.

V. PARITY LIFETIME EXTRACTION PROCEDURE

In this section we elaborate on the analysis method for extracting the characteristic lifetimes of the singlet and doublet states, T_{s} and T_{d}. We start with a continuous measurement at a fixed readout frequency where we monitor the demodulated output signal integrated in time bins of $t_{\text{int}} = 2.3$ μs. This reveals a complex random telegraph signal jumping between two states in the (I,Q)-plane. The histogram of the acquired (I,Q) points shows two states (Fig. S18(a)) whose centers define an axis X. A segment of the measured telegraph signal, projected onto this X axis, is shown in Fig. S18(c). Taking the histogram along this axis results in a double Gaussian distribution (Fig. S18(d)) that is well-described by

$$g(x) = \frac{A_1}{\sqrt{2\pi\sigma^2}} e^{\frac{-(x-x_1)^2}{2\sigma^2}} + \frac{A_2}{\sqrt{2\pi\sigma^2}} e^{\frac{-(x-x_2)^2}{2\sigma^2}} \tag{S11}$$

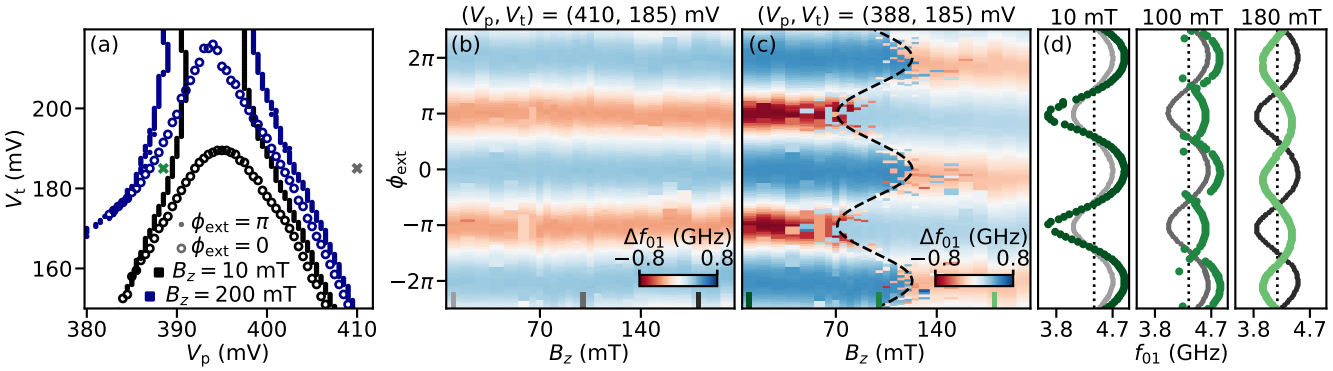

Figure S17. **Data analysis for magnetic field dependence of device A.** (a) Borders between singlet and doublet regions for $B_z = 10\,\mathrm{mT}$ (black) and $B_z = 200\,\mathrm{mT}$ (blue). Solid and empty markers correspond to $\phi_{\mathrm{ext}} = \pi$ and $\phi_{\mathrm{ext}} = 0$, respectively. (b) and (c) show Δf_{01} versus B_z and ϕ_{ext}, measured at the two gate points indicated in (a) with grey and green markers, respectively. In (b), the singlet is the ground state for all B_z. This gate point is used to identify a flux reference for each B_z. For (c), there is a singlet-doublet ground state transition with B_z, where the sinusoidal dashed line serves as a guide for the eye. (d) f_{01} versus ϕ_{ext} for the three B_z values indicated in (b) and (c). The dotted line indicates f_{01}^0, which decreases with B_z as shown in Fig. S10(e).

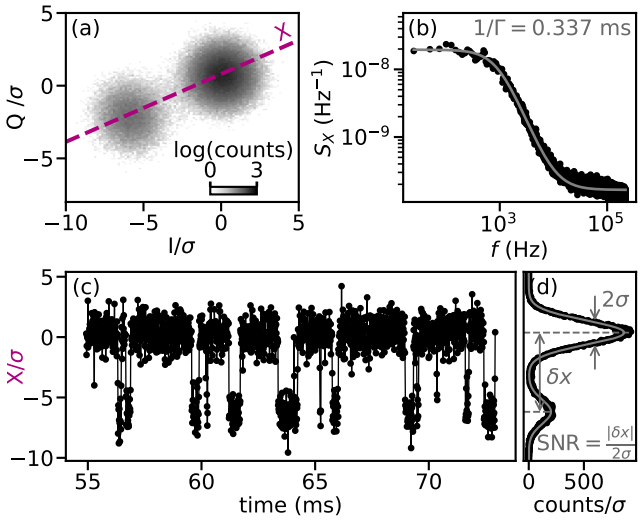

Figure S18. **Parity lifetime analysis.** (a) Logarithmic-scale histogram of the resonator response in the (I,Q)-plane after integrating a 2 s time trace with time bins of $t_{\mathrm{int}} = 11.4\,\mu\mathrm{s}$. It exhibits two separate Gaussian distributions whose centers define an axis, X, indicated with a dashed line. (b) Power spectral density (black) of an unintegrated 2 s time trace projected onto the X axis. In grey, best fit of a Lorentzian lineshape with a white noise background (Eq. (S12)). (c) 18 ms cut of the integrated response projected onto the X axis, revealing jumps between two distinct states. (d) 1D histogram of the response in (a) projected onto the X axis (black) and the best fit of a double Gaussian line-shape (grey, Eq. (S11)). For all panels $V_{\mathrm{L}} = 325\,\mathrm{mV}$, $V_{\mathrm{T}} = -60\,\mathrm{mV}$, $V_{\mathrm{P}} = 551.4\,\mathrm{mV}$, $B_z = 0$ and $\phi_{\mathrm{ext}} = 0$.

Here, $A_{1,2}$ are the relative populations of singlet and doublet occupation, $x_{1,2}$ are the centers of each Gaussian and σ is their standard deviation. For the data shown in Fig. S18, the fit results in $A_1 = 2169\sigma$, $A_2 = 506\sigma$, $x_1 = 0.37\sigma$ and $x_2 = -6.19\sigma$, from which we determine the SNR $= |x_1 - x_2|/2\sigma = 3.28$.

From the time domain information of the signal we construct its power spectral density (PSD), which is its squared discrete Fourier transform (Fig. S18(b))

$$S_X(f) = \frac{\Delta t}{N\pi}\left|\sum_{n=1}^{N} X(n\Delta t)e^{-i2\pi f n\Delta t}\right|^2 \tag{S12}$$

where $X(t)$ is the measured signal (as projected onto the previously defined X-axis), $\Delta t = 2.3\,\mu\mathrm{s}$ is the discrete time bin in which the data is measured, $N = \frac{T}{\Delta t}$ is the number of points and T is the total signal length. In practice we

use Welch's method with a Hanning window [25] to calculate the power spectral density, dividing the trace into 50 sections of length 40 ms that overlap by 20 ms and averaging the power spectral density of all segments. This results in a spectrum that is well fit by a single Lorentzian of the form

$$S(f) = A\frac{4\Gamma}{(2\Gamma)^2 + (2\pi f)^2} + B, \tag{S13}$$

from which we obtain $1/\Gamma = 0.337$ ms, $A = 5.75 \cdot 10^{-5}$ and $B = 1.65 \cdot 10^{-10}$ Hz^{-1}.

Combining the amplitude ratio $R = A_1/A_2$ obtained from the Gaussian fit of the two quadratures and the Γ value obtained from the Lorentzian fit of the PSD, we calculate

$$T_\mathrm{s} = 1/\Gamma_\mathrm{s} = \frac{1+R}{2\Gamma R} \tag{S14}$$

$$T_\mathrm{d} = 1/\Gamma_\mathrm{d} = \frac{1+R}{2\Gamma} \tag{S15}$$

to obtain $T_\mathrm{s} = 0.89$ ms, $T_\mathrm{d} = 0.21$ ms.

VI. EXTENDED PARITY LIFETIME DATA

A. Parity lifetimes linecut versus flux

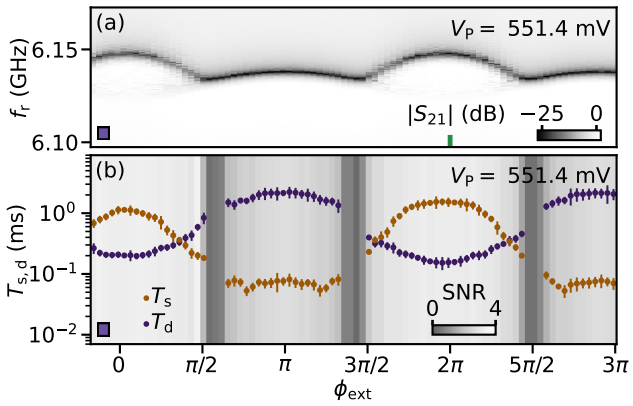

Figure S19. **Flux dependence of parity lifetimes** (a) ϕ_ext dependence of single-tone spectroscopy at $V_\mathrm{P} = 551.4$ mV. (b) ϕ_ext dependence of the parity lifetimes extracted following the analysis in Fig. S18 at $V_\mathrm{P} = 551.4$ mV. Markers indicate the mean and error bars indicate the maximum and minimum values of 10 consecutive 2 s time traces. SNR $= \frac{|\delta x|}{2\sigma}$ is shown in greyscale in the background. For points where SNR < 1, the extracted parity lifetimes are not shown as we do not consider them reliable. Measured at the same V_T , V_L and B_z as for Fig. S18.

Fig. S19 shows the flux dependence of the lifetimes of the singlet and doublet states at $V_\mathrm{P} = 554.4$ mV, which accompanies main text Fig. 7. We find that both singlet and doublet lifetimes show an approximate sinusoidal dependence on the applied flux. As discussed in the main text, this flux dependence most likely originates from the oscillation of the singlet-doublet energy gap with flux. However it could also be indicative of a coherent suppression of the tunneling rates [26]. We further note that the sudden drops in SNR are due to crossings of the transmon frequencies of the singlet and doublet states. At these points both resonator frequencies become indistinguishable and their lifetimes can not be measured.

B. Power and temperature dependence of parity lifetimes

Here we present additional data on the readout power and temperature dependence of the parity lifetimes shown in Fig. 7 of the main text. The power dependence at four selected points across a phase boundary is shown in Figs. S20(c-f). Away from the transition (purple) and right on top of the transition (green) the readout power does not have a

strong effect on the extracted lifetimes in the investigated range. For plunger gate values V_P closer to the transition, however, the asymmetry of the lifetimes decreases with power (blue). Although the origin of this dependence is not clear, we conjecture it is related to parity pumping effects [27].

Temperature dependencies at the same gate points, measured at a readout power of -22 dBm at the fridge input, are shown in Figs. S20(g-j). Here the mixing chamber temperature of the dilution refrigerator is measured with a ruthenium oxide resistance thermometer and increased in a controlled step-wise fashion with a variable-output heater mounted on the mixing chamber plate. We observe different effects of temperature for each of the gate points. In general, there is a temperature independent regime at low temperatures, followed by a temperature dependent drop above a certain characteristic temperature, which varies over tens of mK for different gate points. For some of the gate points, however, the temperature independent contribution is absent and the effect of increased mixing chamber temperature starts immediately at base temperature (Fig. S20(i)). These results are indicative of non-equilibrium effects playing a role in the physics of the devices under study, their exact behaviour dependent on the energy level configuration of the quantum dot junction.

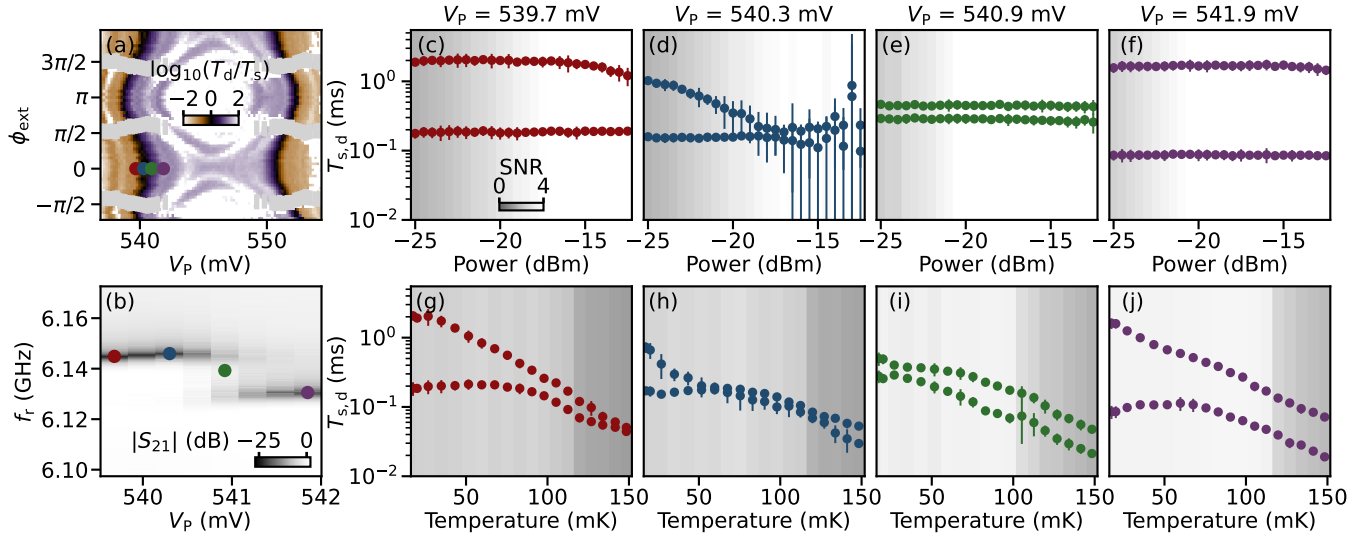

Figure S20. **Power and temperature dependence of parity lifetimes across the singlet-doublet transition** (a) 2D map of $\log_{10}(T_d/T_s)$ versus V_P and ϕ_{ext}, extracted from a 2 s time trace for each pixel. This is the same panel as Fig. 7(e) in the main text. (b) V_P dependence of single-tone spectroscopy at $\phi_{ext} = 0$, across a singlet/doublet transition. For (a) and (b), the mixing chamber temperature is 18 mK and the readout power is −22 dBm. (c-f) Readout power dependence at 18 mK of the extracted parity lifetimes at the plunger points indicated in (a) and (b). Markers indicate the mean and error bars indicate the maximum and minimum values of 10 consecutive 2 s time traces. The SNR is shown in greyscale in the background. For points where SNR < 1, the extracted parity lifetimes are discarded. (g-j) Same as (c-d) but versus temperature and at a power of −22 dBm. All powers are given at the fridge input.

C. Parity lifetimes versus tunnel gate

To complement the data shown in Fig. 7 of the main text, taken at $V_T = -60$ mV, we also show the V_T dependence of the parity lifetimes at $\phi_{ext} = 0$ in Fig. S21. As for device A, the doublet ground state region exhibits a dome shape in V_P and V_T space, and at the transition between singlet and doublet ground states the lifetimes for both states become equal. Away from the transition, the lifetime asymmetry increases and the lifetimes differ by more than one order of magnitude. We note that the gate compensation of device B was not ideal, resulting in a small tilt of the dome.

Similarly to the behaviour shown in the main text for ϕ_{ext} and V_P, in this case we also observe contours of equal ratio where the lifetime asymmetry abruptly increases or decreases. For higher readout power these contours become accentuated, as shown in Fig. S21(c). Furthermore, for higher power the region with similar lifetimes around the ground state transition becomes wider. This is due to the parity lifetimes having a different dependence on power for different regions in gate space. For most regions in gate space there is again almost no dependence on readout power in the range explored (Fig. S21(e,f)). However, on special gate regions, such as close to ground state transitions (Fig. S21(g)) and on top of the observed contours (Fig. S21(d)), the lifetime asymmetry decreases rapidly with power,

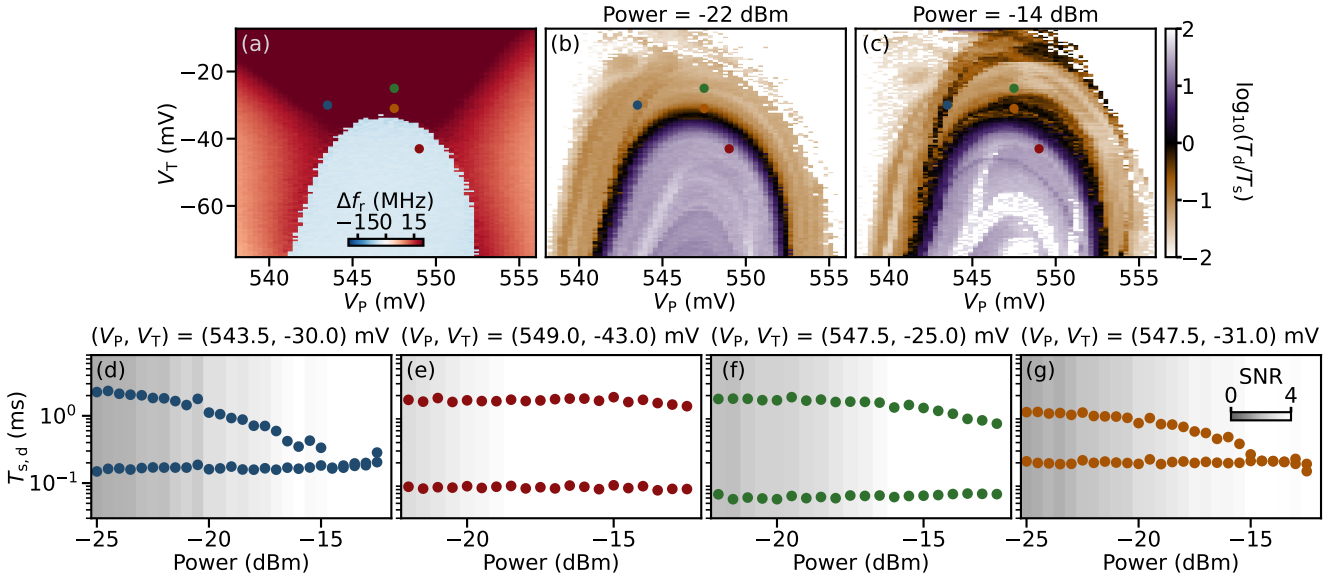

Figure S21. **Tunnel, plunger and power dependence of parity lifetimes** (a) $\Delta f_r = f_{res} - f^0_{res}$ versus V_P and V_T measured at $\phi_{ext} = 0$. It shows a regions of constructive and destructive interference, separated by sharp dome-like boundary. (b) Two-dimensional map of $\log_{10}(T_d/T_s)$ versus V_P and V_T, measured at a power of -22 dBm. (c) Same as (b) but for a power of -14 dBm. (d-e) Power dependence of the extracted parity lifetimes at the gate points indicated in (a-c). All powers are given at the fridge input.

similar to the effect shown in Fig. S20.

[1] V. Meden, The Anderson–Josephson quantum dot—a theory perspective, J. Phys. Condens. Matter **31**, 163001 (2019).
[2] K. G. Wilson, The renormalization group: Critical phenomena and the Kondo problem, Rev. Mod. Phys. **47**, 773 (1975).
[3] H. Krishna-murthy, J. Wilkins, and K. Wilson, Renormalization-group approach to the Anderson model of dilute magnetic alloys. i. static properties for the symmetric case, Phys. Rev. B **21**, 1003 (1980).
[4] K. Satori, H. Shiba, O. Sakai, and Y. Shimizu, Numerical renormalization group study of magnetic impurities in superconductors, J. Phys. Soc. Japan **61**, 3239 (1992).
[5] T. Yoshioka and Y. Ohashi, Numerical renormalization group studies on single impurity Anderson model in superconductivity: a unified treatment of magnetic, nonmagnetic impurities, and resonance scattering, J. Phys. Soc. Japan **69**, 1812 (2000).
[6] R. Bulla, T. A. Costi, and T. Pruschke, The numerical renormalization group method for quantum impurity systems, Rev. Mod. Phys. **80**, 395 (2008).
[7] R. Žitko and T. Pruschke, Energy resolution and discretization artefacts in the numerical renormalization group, Phys. Rev. B **79**, 085106 (2009).
[8] R. Zitko, NRG Ljubljana (2021).
[9] A. Kadlecová, M. Žonda, and T. Novotný, Quantum dot attached to superconducting leads: Relation between symmetric and asymmetric coupling, Phys. Rev. B **95**, 195114 (2017).
[10] R. Zitko, Josephson potentials for single impurity Anderson impurity in a junction between two superconductors, 10.5281/zenodo.5874832 (2022).
[11] J. Koch, T. M. Yu, J. Gambetta, A. A. Houck, D. I. Schuster, J. Majer, A. Blais, M. H. Devoret, S. M. Girvin, and R. J. Schoelkopf, Charge-insensitive qubit design derived from the cooper pair box, Phys. Rev. A **76**, 042319 (2007).
[12] M. D. Schroer, K. D. Petersson, M. Jung, and J. R. Petta, Field tuning the g factor in InAs nanowire double quantum dots, Phys. Rev. Lett. **107**, 176811 (2011).
[13] A. Kringhøj, L. Casparis, M. Hell, T. W. Larsen, F. Kuemmeth, M. Leijnse, K. Flensberg, P. Krogstrup, J. Nygård, K. D. Petersson, and C. M. Marcus, Anharmonicity of a superconducting qubit with a few-mode Josephson junction, Phys. Rev. B **97**, 060508(R) (2018).
[14] A. E. Antipov, A. Bargerbos, G. W. Winkler, B. Bauer, E. Rossi, and R. M. Lutchyn, Effects of gate-induced electric fields on semiconductor Majorana nanowires, Phys. Rev. X **8**, 031041 (2018).
[15] G. W. Winkler, A. E. Antipov, B. van Heck, A. A. Soluyanov, L. I. Glazman, M. Wimmer, and R. M. Lutchyn, Unified numerical approach to topological semiconductor-superconductor heterostructures, Phys. Rev. B **99**, 245408 (2019).

[16] A. Kringhøj, T. W. Larsen, B. van Heck, D. Sabonis, O. Erlandsson, I. Petkovic, D. I. Pikulin, P. Krogstrup, K. D. Petersson, and C. M. Marcus, Controlled DC monitoring of a superconducting qubit, Phys. Rev. Lett. **124**, 056801 (2020).

[17] D. de Jong, C. G. Prosko, D. M. A. Waardenburg, L. Han, F. K. Malinowski, P. Krogstrup, L. P. Kouwenhoven, J. V. Koski, and W. Pfaff, Rapid microwave-only characterization and readout of quantum dots using multiplexed gigahertz-frequency resonators, Phys. Rev. Applied **16**, 014007 (2021).

[18] L. I. Glazman and G. Catelani, Bogoliubov quasiparticles in superconducting qubits, SciPost Phys. Lect. Notes , 31 (2021).

[19] P. Krogstrup, N. L. B. Ziino, W. Chang, S. M. Albrecht, M. H. Madsen, E. Johnson, J. Nygård, C. Marcus, and T. S. Jespersen, Epitaxy of semiconductor-superconductor nanowires, Nat. Mater. **14**, 400 (2015).

[20] J. Wesdorp, L. Grünhaupt, A. Vaartjes, M. Pita-Vidal, A. Bargerbos, L. J. Splitthoff, B. van Heck, and G. de Lange, Andreev spectroscopy of an InAs junction in a magnetic field, In preparation (2022).

[21] F. Luthi, T. Stavenga, O. W. Enzing, A. Bruno, C. Dickel, N. K. Langford, M. A. Rol, T. S. Jespersen, J. Nygård, P. Krogstrup, and L. DiCarlo, Evolution of nanowire transmon qubits and their coherence in a magnetic field, Phys. Rev. Lett. **120**, 100502 (2018).

[22] E. M. Spanton, M. Deng, S. Vaitiekėnas, P. Krogstrup, J. Nygård, C. M. Marcus, and K. A. Moler, Current–phase relations of few-mode InAs nanowire Josephson junctions, Nature Physics **13**, 1177 (2017).

[23] S. Hart, Z. Cui, G. Ménard, M. Deng, A. E. Antipov, R. M. Lutchyn, P. Krogstrup, C. M. Marcus, and K. A. Moler, Current-phase relations of InAs nanowire Josephson junctions: From interacting to multimode regimes, Phys. Rev. B **100**, 064523 (2019).

[24] L. J. Splitthoff, A. Bargerbos, L. Grunhaupt, M. Pita-Vidal, J. Wesdorp, Y. Liu, A. Kou, C. K. Andersen, and B. van Heck, Gate-tunable kinetic inductance in proximitized nanowires, arXiv e-prints (2022), arXiv:2202.08729.

[25] P. Welch, The use of fast fourier transform for the estimation of power spectra: A method based on time averaging over short, modified periodograms, IEEE Transactions on Audio and Electroacoustics **15**, 70 (1967).

[26] I. M. Pop, K. Geerlings, G. Catelani, R. J. Schoelkopf, L. I. Glazman, and M. H. Devoret, Coherent suppression of electromagnetic dissipation due to superconducting quasiparticles, Nature **508**, 369 (2014).

[27] J. J. Wesdorp, L. Grünhaupt, A. Vaartjes, M. Pita-Vidal, A. Bargerbos, L. J. Splitthoff, P. Krogstrup, B. van Heck, and G. de Lange, Dynamical polarization of the fermion parity in a nanowire Josephson junction, arXiv e-prints (2021), arXiv:2112.01936.